Spontaneous polarization of ferroelectric heterostructured nanorod arrays for high-performance photoelectrochemical cathodic protection

Yunpeng Liu [a], Zhenyu Wang [a], Changzheng Lin [a], Juantao Zhang [a], Jiangtao Feng [a*], Bo Hou [b**], Wei Yan [a,c***], Mingtao Li [d] and Zijun Ren [e]

a Department of Environmental Science & Engineering, School of Energy and Power Engineering, Xi'an Jiaotong University, Xi'an, 710049, China. Email: fjtes@xjtu.edu.cn

b School of Physics and Astronomy, Cardiff University, The Parade, Cardiff, CF24 3AA, Wales, UK. Email: HouB6@cardiff.ac.uk

c State Key Laboratory of Multiphase Flow in Power Engineering, School of Energy and Power Engineering, Xi'an Jiaotong University, Xi'an, 710049, China. Email: yanwei@xjtu.edu.cn

d International Research Center for Renewable Energy (IRCRE), State Key Laboratory of Multiphase Flow in Power Engineering (MFPE), Xi'an Jiaotong University, Xi'an, 710049, China

e Instrument Analysis Center of Xi'an Jiaotong University, Xi'an Jiaotong University, Xi'an, 710049, China

Corresponding authors:

Jiangtao Feng: fjtes@xjtu.edu.cn

Bo Hou: HouB6@cardiff.ac.uk

Wei Yan: yanwei@xjtu.edu.cn

Abstract: Corrosion is a critical global problem for the steel industry and a grand challenge toward Net-Zero clean growth. TiO_2 nanorods (TNRs) have been developed for photoelectrochemical cathodic protection (PCP) of coupled metal, however, the performance was hindered by their wide bandgap, weak visible-light response, and low separation efficiency of photocarriers. In this work, a unique multilayered coaxial nanorod array (TNRs/BTO/Ag NPs) structure has been proposed to enhance 'hot' electrons injection via inserting a ferroelectric semiconductor $BaTiO_3$ (BTO) nanolayer between TNRs and Ag nanoparticles (Ag NPs). The spontaneous ferroelectric BTO nanolayer built a polar charge-induced electric field (PEF), resulting in a strong spontaneous polarization. Furthermore, the as-proposed structure can negatively shift the surface potential of the coupling 304 stainless steel by 0.80 V relative to its corrosion potential under simulated solar light illumination which is the record PCP potential among reported works. Based on comprehensive electrochemical and theoretical studies, the origin of the enhanced photogenerated carriers' separation and depletion to the coupled metals is attributed to a synergic effect between PEF (the spontaneous polarization of BTO) and internal electric field (IEF) resulting from the cascade energy band alignment. Various promising applications can be envisioned from as-proposed multilayered coaxial nanorod array photoelectrodes.

Keywords: Photoelectrochemical cathodic protection, Ferroelectric, Surface plasmon resonance, 304 stainless steel, DFT.

Introduction

With the flourished development of the marine economy, the requirement for stainless steel increases yearly due to its low cost and high reliability. Whereas, metal corrosion is a severe problem in the stainless steel industry and corresponding products, particularly in marine and other brine environments.[1] In recent years, many anti-corrosion methods have been proposed, including corrosion inhibits,[2] anti-corrosion coating,[3] and electrochemical protection.[4] Among these technologies, photoelectrochemical cathodic protection (PCP) has been paid increasing attention, owing to its environmentally sustainable and energy-saving advantages.[5] In the PCP system, the photoanode generates the photoexcited electron/hole (e^-/h^+) pairs with light irradiation, and those electrons transfer to the connected electrode to shift the steel's surface potential negatively.[6] Thus, improving the light-response ability of photoelectrode contributes vitally to enhancing PCP efficiency.

As one of the most common photoanode, TiO_2 nanorods (TNRs) film has been utilized in PCP applications owing to its one-dimensional (1D) electron transmission, which could improve the separation of the e^-/h^+ pairs.[7] Nevertheless, the inherent wide bandgap (> 3 eV) of TiO_2 hinders efficient solar light absorption. Hence, many optimization approaches have been developed to overcome this issue, including noble metal loading, metallic ions or non-metal doping, and heterostructure construction.[8] The noble metal nanoparticles (Au, Ag, Pt, Pd, etc.), especially Ag nanoparticles (Ag NPs) loading, is a high-efficiency and low-cost materials to improve the

photoelectrochemical (PEC) efficiency of TNRs.[9]

On the other hand, forming the Schottky barrier between Ag NPs and TiO_2 could hinder the recombination of the e^-/h^+ pairs.[10] More importantly, the surface plasmon resonance (SPR) effect of Ag NPs could expand the light-response range of wide-bandgap semiconductors from UV to visible light.[11] In this process, the photogenerated 'hot' electrons originating from the SPR effect could be injected into a neighboring semiconductor's conduction band (CB) to enhance PEC efficiency.[12] Guan et al.[13] and Li et al.[6] synthesized TiO_2 nanotube film modified with Ag NPs shows PCP performance enhancement for the coupled steel with visible light irradiation. However, the low migration efficiency of 'hot' electrons from Ag NPs to TNRs still hinders the application of TNRs/Ag NPs binary film due to the weakly driving force for photocarriers between Ag and TiO_2, which results in poor photo-to-electron conversion efficiency.[14] Therefore, how to reduce the photocarriers recombination through a built-in potential field in the binary system consisting of TNRs and Ag NPs is vastly considered as a primary challenge in the PCP field.

Internal electric field (IEF) between TNRs and Ag NPs could be a promising solution for e^-/h^+ pairs disassociation and depletion. IEF could be established by ferroelectric polarization, p-n junction, polymorphism junctions, etc.[15] Recently, ferroelectric materials (such as $SrTiO_3$, $LiNbO_3$, $BiFeO_3$, etc.) have been widely employed to generate a polar charge-induced electric field (PEF) and control the charges' separation

in the research field of photocatalysis,[16, 17] LEDs [18] and solar cells.[19] Furthermore, under the mechanical stress- or heat-induced treatment, there are changes in the distribution of free carriers in a neighboring semiconductor material, which results in an efficient charge carrier separation and depletion.[20, 21]

However, due to the distorted spatial structure, ferroelectric $BaTiO_3$ (BTO) could be spontaneously and permanently polarized.[22] Notably, this PEF field could be significantly improved by the existence of ferroelectric heterojunction interfaces [23] and Schottky junction interfaces.[24] Furthermore, spontaneous polarization in those interfaces would induce considerable free carrier redistribution and boost the directed photocarriers separation in the adjacent semiconductors.[25] Therefore, introducing $BaTiO_3$ as an interlayer in the binary system consisting of TNRs and Ag NPs could be a promising strategy to enhance PCP efficiency.

Herein, a multilayered coaxial nanorod array (TNRs/BTO/Ag NPs) is successfully constructed (Scheme 1) as a unique ferroelectric photoanode design for PCP application, exhibiting enhanced PCP efficiency for preventing corrosion for 304 stainless steel (304SS). Spectroscopy and microscopy methods were employed to investigate the crystalline structure, morphology, chemical component and optical properties of the as-prepared composite film. Meanwhile, DFT analysis was utilized to understand the relationship and mechanisms between the multilayered ferroelectric coaxial design and the corresponding remarkable anti-corrosion efficiency.

Results and discussion

Structural characteristics

The Raman analysis of the TNRs/BTO/Ag NPs composite film was applied to study the structural symmetry of composite materials. As shown in Figure 1a, the three peaks (237, 446 and 610 cm^{-1}) marked by spade correspond to rutile TiO_2,[26] and the other peak (715 cm^{-1}) marked by black diamonds corresponds to the BTO.[21] Therefore, the peaks can be identified as the two pure phases for the TNRs/BTO/Ag NPs composite. However, the Raman test cannot detect elemental Ag NPs due to the crystal symmetry of Ag,[27] hence, the presence of Ag NPs will be confirmed by the latter characterizations.

The XRD patterns of the TNRs, TNRs/BTO and TNRs/BTO/Ag NPs composites are displayed in Figure 1b. The clear peaks of TNRs at 27.6°, 36.2°, 41.3°, 54.5°, 63.0° and 70.0° can be attributed to the (1 1 0), (1 0 1), (1 1 1), (2 1 1), (0 0 2) and (1 1 2) planes of rutile TiO_2 (JCPDS No. 65-0912) and the remaining peaks could be assigned to the FTO substrate.[28] The diffraction peak of TNRs/BTO film at ~31.3° was assigned to the (1 0 1) plane of tetragonal BTO (JCPDS No. 05-0626),[25] evidencing the evolution of the BTO layer. After the electro-deposition process, characteristic Ag (1 1 1) and (2 0 0) diffraction peaks at ~38.1° and ~44.3° (JCPDS No. 87-0718) emerged,[29] which indicates the formation of the TNRs/BTO/Ag NPs composite film.

The morphologies of TNRs, TNRs/BTO and TNRs/BTO/Ag NPs composites were

studied by scanning electron microscope (SEM). As shown in Figure 2a, neatly arranged TNRs are vertically grown on the substrate with a diameter of ~150 nm, and the cross-section image (Figure 2d) of the TNRs exhibits that the nanorods' length is 2.5 ± 0.05 μm, and the nanorods are almost vertical to the substrate, which agrees with the previous report.[30] After the formation of the BTO nanolayer via situ ion-exchange method (Figure 2b, e), the morphology (especially thickness and length of nanorods) of the nanorods had no distinct change; meanwhile, the perpendicular 1D nanorod structure implies the formation of TNRs/BTO core/shell nanorod array. After the further loading Ag NPs (Figure 2c, f), it can also be seen that Ag decoration leads to coverage of uniformly-distributed Ag NPs with a diameter of ~15 nm on the surface of the nanorods, which is vital to achieving the SPR effect.

The TNRs/BTO/Ag NPs film microstructure was further investigated by Transmission electron microscopy (TEM) and high-resolution TEM (HRTEM). The typical 1D structure of TNRs/BTO/Ag NPs film can be resolved (Figure 3a). Figures 3b and 3c show spherical Ag NPs with a mean size of ~10 nm. They disperse uniformly on the surface of the nanorods without aggregate, which could generate an enhanced local electromagnetic field due to the SPR effect.[31, 32] The HRTEM image shown in Figure 3d demonstrates three sets of lattice fringes assigned to the TNRs core, BTO shell and Ag NPs. The lattice fringes of ~0.33 nm could be attributed to the (1 1 0) crystal facet of rutile TiO_2, proving the NRs growth along with the <0 0 1> zone axis.[33] The characteristic tetragonal BTO with a d_{111} lattice fringe (~0.23 nm) could also be

readily indexed.[34] The BTO shell has a thickness of ~7.60 nm, which is thicker than BTO's critical thickness (~2.4 nm) for ferroelectricity at room temperature.[35] Meanwhile, the lattice fringes of 0.24 nm can be resolved, which is assigned to (1 1 1) planes of cubic Ag. Additionally, as displayed in the EDS mapping images of TNRs/BTO/Ag NPs (Figure S1), Ti, O and Ba elements are the main constituents of nanorods. In contrast, Ag elements are uniformly distributed on the surface of the nanorods.

As shown in Figure 4, the XPS analysis is utilized to study the chemical composition of as-prepared films. The full scan survey XPS spectrum of the TNRs/BTO/Ag NPs film is displayed in Figure 4a, displaying Ti 2p, O 1s, Ba 3d and Ag 3d peaks. As shown in the Ti 2p spectrum of TNRs (Figure 4b), the two sharp peaks (Ti $2p_{1/2}$ and Ti $2p_{3/2}$) could be deconvoloved.[36] Through in situ ion-exchange methods, the location of two characteristic peaks is more negative than those of pure TNRs, implying the embedment of Ba^{2+} in the subsurface of the TNRs film. Meanwhile, the continuous negative shift of the two Ti 2p peaks from the TNRs/BTO curve to the TNRs/BTO/Ag NPs curve demonstrates the existence of charge transfer among Ag NPs, BTO nanolayer, and TNRs.[37] O's 1s orbital absorption peaks can be decomposed into three peaks (Figure 4c). The main peak at 530.5 eV is attributed to lattice oxygen bonds, and a peak at 531.6 eV can be attributed to oxygen vacancies, whereas the peak at 532.8 eV is related to the surface hydroxyl group.[38] As shown in Figure 4d, the two characteristic peaks at 794.8 eV and 779.6 eV were assigned to Ba $3d_{3/2}$ and Ba $3d_{5/2,}$ respectively, which

agrees with the reported Ba 3d in BTO.[39] As shown in Figure 4c, the peaks at 367.7 eV and 373.7 eV can be assigned to Ag $3d_{5/2}$ and Ag $3d_{3/2}$, respectively,[40] confirming the successful loading of metallic Ag on the surface of the composite. As shown in XPS valence band (VB) characterization (Figure S2), the VB edge of TNRs/BTO/Ag NPs is more negative than that of pure TNRs, owing to the formation of heterostructures.[41]

The UV-visible diffuse reflectance spectra (DRS) of the TNRs, TNRs/BTO and TNRs/BTO/Ag NPs films are displayed in Figure S3a. The TNRs and TNRs/BTO films have weak absorbance in the visible spectra due to their wide bandgap.[42] In contrast, the TNRs/BTO/Ag NPs composite shows improved visible-light response-ability, resulting from the SPR effect of spatially confined electrons in the Ag NPs.[10] Hence, loading Ag NPs on TNRs/BTO film could enhance the light absorption ability, particularly for visible light. Figure S3b displays the PL spectra of TNRs, TNRs/BTO and TNRs/BTO/Ag NPs composite excites at about 330 nm. PL emission spectra of all samples show four main peaks at 414, 437, 459 and 485 nm, separately. Especially, the distinct broad PL emission peak located at 459 nm is triggered by the recombination of the e^-/h^+ pairs. The TNRs/BTO/Ag NPs composites exhibit the weakest PL emission peak, which means introducing ferroelectric BTO interlayers could improve the dissociation and depletion of photo-induced charge carriers.

PCP performances

The PEC tests are employed to evaluate the enhanced PCP performance of the

TNRs/BTO/Ag NPs film. Figure 5a displays the influence of the hydrothermal reaction time of the BTO nanolayer on the photocurrent density when 304SS is connected with the as-prepared films. As shown in Figure 5a, when the photoanodes were irradiated, all the composites' photocurrents were positive, demonstrating the migration of photoexcited electrons from the photoelectrode to the coupled metal.[43] The photocurrent densities display the following rank: TNRs/BTO-6 h (0.97 $mA \cdot cm^{-2}$) > TNRs/BTO-4 h (0.78 $mA \cdot cm^{-2}$) > TNRs/BTO-8 h (0.71 $mA \cdot cm^{-2}$) > TNRs/BTO-2 h (0.49 $mA \cdot cm^{-2}$) > TNRs (0.39 $mA \cdot cm^{-2}$). The BTO-modified TNRs show a higher photocurrent density than that of pristine TNRs film, proving that the BTO interlayer could increase the photoresponse ability of TNRs under solar illumination. Meanwhile, the photocurrent density of 304SS connected with TNRs/BTO binary film shows significant enhancement with the biggest photocurrent (0.97 $mA \cdot cm^{-2}$) generated from a 6 h hydrothermal grown TNRs/BTO sample.

Figure 5b shows the open-circuit potential (OCP) changes of 304SS in 3.5 wt% NaCl solution. Without connected with photoelectrodes, the 304SS' self-corrosion potential is about -0.16 V vs. Ag/AgCl. After being connected with the photoelectrodes in darkness, all 304SS' surface potential shifts below its self-corrosion potential because of the galvanic effect.[44] When the photoanodes are irradiated with simulated solar light, all the OCP values quickly drop to more negative values, and it could be assigned to the 304SS' cathodic polarization because of the transfer of photocarriers from the films to the coupled metal.[45] Usually, the more negative OCP value of the coupled

steel represents better anti-corrosion efficiency.[46] The OCP values of different samples can be ranked as follows: TNRs/BTO-6 h (-0.64 V vs. Ag/AgCl) < TNRs/BTO-4 h (-0.60 V vs. Ag/AgCl) < TNRs/BTO-8 h (-0.58 V vs. Ag/AgCl) < TNRs/BTO-2 h (-0.55 V vs. Ag/AgCl) < TNRs (-0.51 V vs. Ag/AgCl). Hence, all the OCP values of the TNRs/BTO binary were more negative than TNRs, indicating the formation of IEF and PEF in the TNRs/BTO interface: i) the IEF resulting from interlaced band energy band could improve the immigration rate of electrons in heterojunction interface. ii) spontaneous ferroelectric polarization property of BTO nanolayer could form the PEF from BTO to TNRs, further boosting the photocarriers separation. Meanwhile, when the hydrothermal time of TNRs/BTO films was increased from 2 h to 6 h, it showed a gradual decrease in OCPs values (TNRs/BTO-6 h exhibited the optimal protection performance, and thus "TNRs/BTO" herein refers to TNRs/BTO-6 h unless otherwise stated), which might be assigned to the increasing PEF and IEF effect with the increasing thickness of BTO shell. However, the inferior OCP value could be observed when the hydrothermal conversion time was further increased to 8 h. It should be noted that thick BTO layers (Figure S4) weakened the tunnelling rate of photogenerated holes. Besides, the non-negligible resistance of the BTO shell would drastically affect the obstacle hole immigrant from the TNRs core,[25] and photoresponse performance would be assigned mainly to the light response-ability from BTO itself.

As shown in Figure 5c, the photocurrent values show the following pattern:

TNRs/BTO/Ag NPs-150 cycles (3.34 $mA \cdot cm^{-2}$) > TNRs/BTO/Ag NPs-200 cycles (2.54 $mA \cdot cm^{-2}$) > TNRs/BTO/Ag NPs-100 cycles (2.19 $mA \cdot cm^{-2}$) > TNRs/BTO/Ag NPs-50 cycles (1.40 $mA \cdot cm^{-2}$) > TNRs/BTO (0.97 $mA \cdot cm^{-2}$). The photocurrent density of 304SS coupled with all the ternary TNRs/BTO/Ag NPs is higher than that of binary TNRs/BTO composite, and it is contributed to the remarkable visible-light response ability of Ag NPs. Especially when the cycle amount of the electro-deposition method is 150, the photocurrent density between TNRs/BTO/Ag NPs-150 cycles film and 304SS increases to 3.34 $mA \cdot cm^{-2}$.

As shown in Figure 5d, the OCP values of different samples can be ranked as follows: TNRs/BTO/Ag NPs-150 cycles (-0.96 V vs. Ag/AgCl) < TNRs/BTO/Ag NPs-200 cycles (-0.85 V vs. Ag/AgCl) < TNRs/BTO/Ag NPs-100 cycles (-0.83 V vs. Ag/AgCl) < TNRs/BTO/Ag NPs-150 cycles (-0.75 V vs. Ag/AgCl) < TNRs/BTO (-0.64 V vs. Ag/AgCl). It is clear that the OCPs values of 304SS connected with all the ternary TNRs/BTO/Ag NPs composite film decrease below -0.75 V vs. Ag/AgCl under simulated solar irradiation, which is lower than that of the TNRs/BTO film. After the deposition of Ag NPs on the surface of TNRs/BTO composite, the plasmon-excited 'hot' electrons in the Ag NPs can be migrated to the neighboring material and metal, which produces a more negative surface potential. Meanwhile, a Schottky barrier would be formed in the BTO/Ag NPs interface, which could remarkably avoid recombining the e^-/h^+ pairs generated from the SPR effect. Additionally, OCPs values of 304SS connected with the as-prepared TNRs/BTO/Ag NPs composite films decreases and then

increase with the cycle amount of the electro-deposition method, i.e. there is the lowest potential (-0.96 V vs. Ag/AgCl) when the cycle amount of electro-deposition method is 150 ("TNRs/BTO/Ag NPs" herein is TNRs/BTO/Ag NPs-200 cycles unless otherwise stated). It should be noted that different amounts of Ag deposition can result in different SPR effects. As shown in Figure S5, when the electro-deposition cycle increases to a certain extent, there is a massive aggregation of Ag NPs on the surface of nanorods, which would decrease the SPR effect of Ag NPs with illumination.[47]

To further investigate the anti-corrosion performance of the above composites in the PCP system, Figure S6 exhibits the Tafel curves of bare 304SS and 304SS connected with the as-prepared photoanode with illumination. The corrosion potential (E_{corr}) of 304SS coupled with photoanodes show more negative values (-0.48 to -0.91 V vs. Ag/AgCl) than that of unconnected 304SS (-0.17 V vs. Ag/AgCl) with illumination, in which E_{corr} of 304SS connected with TNRs/BTO/Ag NPs composite shows the lowest value (-0.91 V vs. Ag/AgCl). Usually, the higher the corrosion current (j_{corr}) value, the more efficient corrosion resistance is.[48] Meanwhile, the j_{corr} of TNRs/BTO/Ag NPs/304SS (123.03 $\mu A \cdot cm^{-2}$) is higher than those of the other films/304SS (24.55 $\mu A \cdot cm^{-2}$ to 58.34 $\mu A \cdot cm^{-2}$) and unconnected 304SS (3.47 $\mu A \cdot cm^{-2}$). This Tafel result indicates that the photo-to-electron conversion efficiency of TNRs/BTO/Ag NPs film is higher than those of TNRs/BTO composite and pure TNRs composite, and more photocarriers can be migrated to the coupled metal under illumination, which is consistent with the above OCP discussion

As representative carbon steel, 65Mn carbon steel (65Mn CS) was also coupled with photoelectrodes to study their PCP performance. The OCP values of the 65Mn CS, coupled with the pristine TNRs (-0.72 V vs. Ag/AgCl) or TNRs/BTO/Ag NPs (-0.97 V vs. Ag/AgCl) (Figure S7), are more negative than its self-corrosion potential (-0.57 V vs. Ag/AgCl), implying that the TNRs/BTO/Ag NPs film could avoid the corrosion of carbon steel. In contrast with previously reported photoelectrodes (Table S1), the ternary TNRs/BTO/Ag NPs composite exhibited remarkable anti-corrosion efficiency.[38, 40, 49-55]

Electrochemical impedance spectroscopy (EIS) has been generally employed to investigate the photoelectron-immigration process of photoelectrode because it is sensitive to electron migration.[56] Figure 5e shows the Nyquist plots of the above composites (TNRs, TNRs/BTO and TNRs/BTO/Ag NPs composite) with irradiation. Only one impedance arc can be seen from each Nyquist plot, and the Bode plots (Figure 5f) display that all those electrodes have two peaks, so the two-time-constant equivalent circuit for the EIS result is used in the set, which is inserted in Figure 5e. As shown in Table S2, the TNRs/BTO/Ag NPs film shows the lowest R_{ct} value (4.55 kΩ·cm^2), in contrast with the other samples (10.48 and 42.38 kΩ·cm^2). In addition, the trinary film also exhibits the smallest $|Z|_{0.01Hz}$, as shown in Figure 5f. The smallest R_{ct} and $|Z|_{0.01Hz}$ of the trinary TNRs/BTO/Ag NPs composite imply the outstanding separation and immigration rate of interfacial photocarriers, resulting from the formation of IEF and

PEF.[57] These electrons could migrate quickly to the connected metal resulting in an improved PCP efficiency.

To further understand the enhanced PCP mechanism of TNRs/BTO/Ag NPs film for coupled steel, the Mott-Schottky (MS) plots of TNRs, TNRs/BTO and TNRs/BTO/Ag NPs films were tested Figure S8. All the MS plots of composites have a positive slope, implying photoanodes' n-type properties. For n-type semiconductors, the flat band potential is relative to its internal electric-field strength.[58] Usually, the more negative the flat band potential, the more significant internal electric-field strength is. Therefore, the flat band potential of TNRs/BTO/Ag NPs film is more negative than those of TNRs and TNRs/BTO films, indicating the stronger driving force to separate the e^-/h^+ pairs.[36] Additional, there is a negative correlation between the carrier's density and the slope of the MS plot.[59] Therefore, the curve slope of TNRs/BTO/Ag NPs composite is more negative than those of TNRs and TNRs/BTO composite, implying a higher free carrier density of TNRs/BTO/Ag NPs, and exhibiting its superior PEC and PCP performances.

To further verify the spontaneous ferroelectric polarization effect of BTO nanolayer in the enhanced PCP performance of TNRs/BTO/Ag NPs photoanode, the high-resolution XPS spectra of Ba 3d in BTO, TNRs/BTO and TNRs/BTO/Ag NPs were conducted. As shown in Figure 6a, the two characteristic peaks could be attributed to Ba $3d_{3/2}$ and Ba $3d_{5/2}$. Compared with the pure BTO, the Ba 3d peaks shift to higher

binding energy for both TNRs/BTO and TNRs/BTO/Ag NPs, which might be attributed to the spontaneous ferroelectric polarization of BTO nanolayer triggers the electrical band bending of TiO_2 to the immigration of photogenerated holes from TiO_2 to BTO.[24, 60] To further study the improved PCP efficiency of TNRs/BTO/Ag NPs via the spontaneous ferroelectric property of BTO, the TNRs/BTO/Ag NPs film was polarized in the positive direction under an external bias (+2 V vs. Ag/AgCl) before the linear sweep voltammetry (LSV) measurement, and a negative polarization (-2 V vs. Ag/AgCl) was also conducted as a reference. As shown in Figure 6b, after positive poling (i.e., the orientation of more ferroelectric domains in the BTO nanolayer is from the photoanode surface to the electrolyte), the photocurrent density of the TNRs/BTO/Ag NPs film was further improved, in contrast with the no-poling counterpart. This is because of the more well alignment of the spontaneously oriented dipoles along the direction of the external electric field.[61] On the other hand, the photogenerated current of the TNRs/BTO/Ag NPs film after negative polarization displayed a significant decay because of the reverse alignment direction of the ferroelectric domains in the BTO nanolayer.[62] The changes in photogenerated current for the TNRs/BTO/Ag NPs film under positive and negative polarization unquestionably demonstrated the effect of the ferroelectric BTO nanolayer on the photoanode. The piezoelectric force microscopy (PFM) test was used to characterize the piezoelectric responses of the TNRs/BTO/Ag NPs film. As shown in Figure S9a, typical morphological features of the TNRs/BTO/Ag NPs film agree with that seen with SEM and TEM. As shown in Figure S9b, the yellow and black areas in the PFM phase images

with strong contrast even in the absence of bias voltage indicate upward-oriented domains, indicating spontaneous ferroelectric polarization across the BTO nanolayer, where separation of e^-/h^+ can be improved. Meanwhile, the closed polarization-electric hysteresis loop (Figure S10) of the TNRs/BTO/Ag NPs film with a remnant polarization of 0.057 $\mu C \cdot cm^{-2}$ also confirmed its ferroelectric property.

The stability evaluation of TNRs/BTO/Ag NPs composite films

The long-term cycles test under light intermission was studied to investigate the stability of TNRs/BTO/Ag NPs hybrid composite film in a PCP system (Figure 7a). The 304SS' OCP value (about -0.93 V vs. Ag/AgCl) is still negative than its initial value (about -0.29 V vs. Ag/AgCl) after intermittent eight hours' simulated solar light irradiation. The variation of crystalline structure and elementary composition of the TNRs/BTO/Ag NPs has been studied after the above stability test. As shown in Figures 7b and c, SEM analysis confirmed no damage was observed to the 1D electron transmission shortcut after a long-time test, and the rarely Ag NPs fall off or gather on the surface of nanorods. Due to the Ag NPs being easily oxidized and thus leading to the decrease of SPR effect, the exemplified XPS spectra of Ag 3d of the composite film after 8 hours' PCP test were also carried out. As shown in Figure 7d, the two characteristic peaks could also be assigned to Ag $3d_{3/2}$ and Ag $3d_{5/2}$ for the composite after 8 hours' test, and no obvious shift and no new peak could be observed compared with that of the composite before the test. Meanwhile, the stability of the BTO interlayer in the composite film is essential for the spontaneous ferroelectric polarization effect.

As shown in Figure S11, the normal thickness of the BTO layer could be still observed clearly, and the EDS spectrum (Figure S12) reveals Ba elements after the stability experiment. Meanwhile, the XRD analysis of the TNRs/BTO/Ag NPs film before and after the stability study (Figure S13) also demonstrates an inappreciable change in peak location and intensity for BTO and Ag NPs.

Mechanism

The charge transfer pathway deeply affects the PCP performance, thus band structure was analyzed by calculating work function (W) via density functional theory (DFT). As displayed in Figures 8a, b and c, the calculated W values of pure Rutile TiO_2, BTO and Ag were 5.014, 5.177 and 5.496 eV, respectively. In general, W was a discrepancy between Fermi level (E_f) and vacuum level. The above data indicated that the E_f of BTO was higher than Ag while lower than Rutile TiO_2 (Figure S14a). The difference between the W and E_f results in charge migration when the two interfaces contact. Therefore, after the interface contact each other (Figure S14b), charges of BTO would transfer to Ag to achieve E_f balance, resulting in the upward bent band of BTO in the BTO/Ag interface, and then the Schottky barrier is formed. This barrier formatted between BTO and Ag effectively avoids the charge backflow from Ag to BTO, hence inhibiting carriers' recombination and prolonging the photocarriers' lifetime. Since BTO loses electrons, its contact interface carries positive charges, thus forming the IEF in BTO/Ag interface. As for the TiO_2/BTO contact interface, charge transfer from TiO_2 to BTO until E_f reaches dynamic equilibrium. This causes the VB (2.31 V vs. the normal hydrogen electrode, NHE) and CB (-0.83 V vs. NHE) [63] of BTO in the TiO_2/BTO

interface to bend downward, while the VB (2.94 V vs. NHE) and CB (-0.16 V vs. NHE) [30] of Rutile TiO_2 bend upward. Rutile TiO_2 has a positive charge at this contact surface, and BTO has a negative charge, thus creating the IEF in TiO_2/BTO interface.

As shown in Scheme 2, under simulated solar light illumination, 'hot' electrons originated from the SPR decay processes of Ag NPs had enough capacities to overcome the Schottky barrier energy (Φ_1) and migrate to the neighboring BTO nanolayer and benefited the photocarriers' transfer. The holes would transfer to the Ag NPs' surface in opposite directions. Meanwhile, under the driving force of IEF, the photogenerated electrons originated from BTO, and 'hot' electrons migrated from Ag NPs would then transfer from the BTO CB to the TiO_2 CB. And the photoexcited holes in TiO_2 transfer inversely to the BTO VB. More importantly, a constant driving force inspired by the polarized charges at the opposite sides of the interfacial ferroelectric nanolayer originating from the spontaneous orienting alignment of polar dipoles could effectively influence the charge transport, which is also the other essential reason for the enhanced PCP performance. Due to the introduction of the BTO interlayer as an electron relay, there would be a spontaneous PEF in TNRs/BTO interface and BTO/Ag NPs interface with the positive charges facing Ag NPs and the negative charge facing TNRs. The strong and endurable driving force would induce upward band bending, increase the depletion region's width in TNRs/BTO interface, and reduce the band level of BTO contacted with Ag (Schottky barrier energy decreased from Φ_1 to Φ_2). It would benefit the hot-electron migration from Ag NPs to BTO and the photoexcited electrons from

BTO to TNRs. Meanwhile, it also helps the migration of photoexcited holes from TNRs to BTO and decreases the recombination of photocarriers. Finally, this film exhibited the dual electric fields (PEF and IEF) from the TNRs/BTO interface toward the BTO/Ag NPs interface. These electrons would be migrated and assumed to the surface of coupled steel effectively, realizing the good PCP performance. Meanwhile, the photogenerated holes from the surface of BTO and Ag NPs would react with OH^- (OH^-/·OH, 1.9 V vs. NHE) [64] to generate ·OH.

Conclusion

We successfully synthesize an efficient polarization charge-improved PCP photoanode under solar light reactivity by employing a ferroelectric BTO nanolayer between TNRs and Ag NPs. More interestingly, the ferroelectric intercalator could form the spontaneous PEF in interfaces, decreasing the Schottky barrier energy in BTO/Ag NPs interface and increasing the width of the depletion region in TNRs/BTO interface. These strong driving forces could promote the separation of photocarriers. Thus, 'hot' electrons originated from Ag NPs, and the photoexcited electrons of BTO and TNRs could all migrate to the surface of the coupled metal. The as-prepared composite compound semiconductor films can achieve a remarkable PCP efficiency for 304SS in 0.5 $mol \cdot L^{-1}$ NaCl solution than the pristine TNRs film under solar light irradiation. We believe that the as-proposed ferroelectric TNRs/BTO/Ag NPs composite functional film can be a promising photoanode not only for the PCP system but also for photocatalysis and other photo-induced energy conversion system.

Experimental

The particulars of chemicals, characterizations, PCP test and the DFT computational method were introduced in the Supporting Information (SI).

Synthesis method

Synthesis of TNRs film: TNRs film was fabricated by the hydrothermal reaction according to our previous work.[65]

Synthesis of TNRs/BTO film: TNRs/BTO core-shell composite was synthesized by locally converting rutile-TiO_2 via a hydrothermal reaction. Firstly, 0.75 mmol $Ba(OH)_2 \cdot 8H_2O$ was added to a sealed Teflon-lined stainless steel autoclave (50 mL) with 5 mL diethylene glycol (DEG), 5 mL ethanol, 1.5 mL 2-propanol, 0.6 g tetrabutylammonium hydroxide solution (TBAH, 40 wt%), and 7 mL deionized water. After stirring for 30 min, the TNRs film was immersed in the above autoclave. The container was sealed and then transferred to the oven and reacted at 180 ℃ for 2-8 h (TNRs/BTO-2 h, TNRs/BTO-4 h, TNRs/BTO-6 h and TNRs/BTO-8 h). After cooling down to room temperature, the films were washed with deionized water and dried naturally in the air

Synthesis of TNRs/BTO/Ag NPs film: The pulse current electro-deposition method was utilized to load Ag NPs onto the TNRs/BTO film using an electrochemical workstation. The deposition solution consisted of 20 $mmol \cdot L^{-1}$ $AgNO_3$ and 100 $mmol \cdot L^{-1}$ $NaNO_3$. The depositions were performed in the two-electrode cell with the TNRs/BTO film as a working electrode and platinum as a counter electrode. A pulse-

current density, pulse duration and on/off time ratio were set at 10 $mA \cdot cm^{-2}$, 1s and 1:3 (s), respectively. To study the loading amount of Ag NPs, the cycle amount of electro-deposition method is verified from 50 to 200 (TNRs/BTO/Ag NPs-50 cycles, TNRs/BTO/Ag NPs-100 cycles, TNRs/BTO/Ag NPs-150 cycles and TNRs/BTO/Ag NPs-200 cycles). The sample was washed with deionized water and then dried naturally in the air.

Acknowledgements

This work was supported by the National Natural Science Foundation of China (Grant No. 21507104) and the Royal Society IEC\NSFC\211201-International Exchanges 2021 Cost Share (NSFC).

Reference

[1] X. Wang, H. Xu, Y. Nan, X. Sun, J. Duan, Y. Huang, B. Hou, Research progress of TiO_2 photocathodic protection to metals in marine environment, J. Oceanol. Limnol. 38 (2020) 1018-1044.

[2] M.R. Ortíz, M.A. Rodríguez, R.M. Carranza, Effect of crevice corrosion inhibitors on the passivity of alloy 22, J. Electrochem. Soc. 159 (2012) C469.

[3] H.D. Johansen, C.M. Brett, A.J. Motheo, Corrosion protection of aluminium alloy by cerium conversion and conducting polymer duplex coatings, Corros. Sci. 63 (2012) 342-350.

[4] P. Refait, M. Jeannin, R. Sabot, H. Antony, S. Pineau, Corrosion and cathodic protection of carbon steel in the tidal zone: Products, mechanisms and kinetics, Corros. Sci. 90 (2015) 375-382.

[5] J. Zhang, R.-G. Du, Z.-Q. Lin, Y.-F. Zhu, Y. Guo, H.-Q. Qi, L. Xu, C.-J. Lin, Highly efficient CdSe/CdS co-sensitized TiO_2 nanotube films for photocathodic protection of stainless steel, Electrochim. Acta, 83 (2012) 59-64.

[6] H. Li, X.T. Wang, Y. Liu, B.R. Hou, Ag and SnO_2 co-sensitized TiO_2 photoanodes for protection of 304SS under visible light, Corros. Sci. 82 (2014) 145-153.

[7] J. Hu, Z.-C. Guan, Y. Liang, J.-Z. Zhou, Q. Liu, H.-P. Wang, H. Zhang, R.-G. Du, Bi_2S_3 modified single crystalline rutile TiO_2 nanorod array films for photoelectrochemical cathodic protection, Corros. Sci. 125 (2017) 59-67.

[8] D. Xu, Y. Liu, Y. Liu, F. Chen, C. Zhang, B. Liu, A review on recent progress in the development of photoelectrodes for photocathodic protection: Design, properties, and prospects, Mater. Des. 197

(2021) 109235.

[9] Y. Wang, M. Zhang, J. Li, H. Yang, J. Gao, G. He, Z. Sun, Construction of Ag@AgCl decorated TiO_2 nanorod array film with optimized photoelectrochemical and photocatalytic performance, Appl. Surf. Sci. 476 (2019) 84-93.

[10] S. Xu, Z. Liu, M. Zhang, L. Guo, Piezotronics enhanced photocatalytic activities of Ag-$BaTiO_3$ plasmonic photocatalysts, J. Alloys Compd. 801 (2019) 483-488.

[11] Y. Wang, M. Zhang, H. Yu, Y. Zuo, J. Gao, G. He, Z. Sun, Facile fabrication of Ag/graphene oxide/TiO_2 nanorod array as a powerful substrate for photocatalytic degradation and surface-enhanced Raman scattering detection, Appl. Catal., B 252 (2019) 174-186.

[12] K.K. Paul, P.K. Giri, Role of Surface Plasmons and Hot Electrons on the Multi-Step Photocatalytic Decay by Defect Enriched Ag@TiO_2 Nanorods under Visible Light, J. Phys. Chem. C 121 (2017) 20016-20030.

[13] Z.-C. Guan, P. Jin, Q. Liu, X. Wang, L.-F. Chen, H. Xu, G.-L. Song, R.-G. Du, Carbon quantum dots/Ag sensitized TiO_2 nanotube film for applications in photocathodic protection, J. Alloys Compd. 797 (2019) 912-921.

[14] X. Zhang, M. Ge, J. Dong, J. Huang, J. He, Y. Lai, Polydopamine-inspired design and synthesis of visible-light-driven Ag NPs@C@elongated TiO_2 NTs core–shell nanocomposites for sustainable hydrogen generation, ACS Sustainable Chem. Eng. 7 (2018) 558-568.

[15] X. Yu, S. Wang, X. Zhang, A. Qi, X. Qiao, Z. Liu, M. Wu, L. Li, Z.L. Wang, Heterostructured nanorod array with piezophototronic and plasmonic effect for photodynamic bacteria killing and wound healing, Nano Energy, 46 (2018) 29-38.

[16] J. Huang, Y. Wang, X. Liu, Y. Li, X. Hu, B. He, Z. Shu, Z. Li, Y. Zhao, Synergistically enhanced charge separation in $BiFeO_3$/Sn:TiO_2 nanorod photoanode via bulk and surface dual modifications, Nano Energy, 59 (2019) 33-40.

[17] S. Xu, L. Guo, Q. Sun, Z.L. Wang, Piezotronic Effect Enhanced Plasmonic Photocatalysis by AuNPs/$BaTiO_3$ Heterostructures, Adv. Funct. Mater. 29 (2019) 1808737.

[18] Y. Cho, S. Pak, B. Li, B. Hou, S. Cha, Enhanced Direct White Light Emission Efficiency in Quantum Dot Light-Emitting Diodes via Embedded Ferroelectric Islands Structure, Adv. Funct. Mater. 31 (2021) 2104239.

[19] Y. Cho, B. Hou, P. Giraud, S. Pak, S. Cha, Ferroelectric Field Effect Induced Charge Carrier Transport Modulation at Quantum Dot Solar Cell Heterojunction Interface, ACS Appl. Energy Mater. 4 (2021) 12056-12062.

[20] W. Zhao, Q. Zhang, H. Wang, J. Rong, L. E, Y. Dai, Enhanced catalytic performance of Ag_2O/$BaTiO_3$ heterostructure microspheres by the piezo/pyro-phototronic synergistic effect, Nano Energy, 73 (2020) 104783.

[21] J. Wu, W. Wang, Y. Tian, C. Song, H. Qiu, H. Xue, Piezotronic effect boosted photocatalytic performance of heterostructured $BaTiO_3$/TiO_2 nanofibers for degradation of organic pollutants, Nano Energy, 77 (2020) 105122.

[22] Y. Wang, L. Liu, W. Zhao, R. Ma, J. Pang, D. Hu, Z. Dou, M. Song, T. Li, K. Miao, Spontaneous polarisation of ferroelectric $BaTiO_3$/ZnO heterostructures with enhanced performance in a Fenton-like catalytic reaction, Ceram. Int. 48 (2022) 2726-2735.

[23] Y. Liu, Y.-L. Zhu, Y.-L. Tang, Y.-J. Wang, Y.-X. Jiang, Y.-B. Xu, B. Zhang, X.-L. Ma, Local Enhancement of Polarization at $PbTiO_3$/$BiFeO_3$ Interfaces Mediated by Charge Transfer, Nano Lett. 17 (2017) 3619-3628.

[24] X. Cheng, Y. Zhang, Y. Bi, Spatial dual-electric fields for highly enhanced the solar water splitting of TiO_2 nanotube arrays, Nano Energy, 57 (2019) 542-548.

[25] W. Yang, Y. Yu, M.B. Starr, X. Yin, Z. Li, A. Kvit, S. Wang, P. Zhao, X. Wang, Ferroelectric Polarization-Enhanced Photoelectrochemical Water Splitting in TiO_2-$BaTiO_3$ Core-Shell Nanowire Photoanodes, Nano Lett, 15 (2015) 7574-7580.

[26] P. Soundarrajan, K. Sankarasubramanian, T. Logu, K. Sethuraman, K. Ramamurthi, Growth of rutile TiO_2 nanorods on TiO_2 seed layer prepared using facile low cost chemical methods, Mater. Lett., 116 (2014) 191-194.

[27] E.H. Alsharaeh, T. Bora, A. Soliman, F. Ahmed, G. Bharath, M.G. Ghoniem, K.M. Abu-Salah, J. Dutta, Sol-Gel-Assisted Microwave-Derived Synthesis of Anatase Ag/TiO_2/GO Nanohybrids toward Efficient Visible Light Phenol Degradation, Catalysts, 7 (2017) 133.

[28] S. Zuo, Z. Liu, W. Liu, X. Li, Z. Li, C. Yao, Q. Chen, Y. Fu, TiO_2 nanorod arrays on the conductive mica combine photoelectrochemical cathodic protection with barrier properties, J. Alloys Compd. 776 (2019) 529-535.

[29] H. Li, X. Wang, Q. Wei, X. Liu, Z. Qian, B. Hou, Enhanced photocathodic protection performance of Ag/graphene/TiO_2 composite for 304SS under visible light, Nanotechnology, 28 (2017) 225701.

[30] Y. Liu, J. Zhu, Z. Wang, X. Yan, J. Zhang, W. Zhang, H. Xu, F. Marken, J. Feng, B. Hou, W. Yan, M. Li, Z. Ren, Towards energy level cascaded “quantum armours” combating metal corrosion, Appl. Surf. Sci. 593 (2022) 153369.

[31] Y. Chen, J. Cao, H. Wei, Z. Wu, X. Wang, Y. Pei, Synthesis of polyvinyl alcohol/Ag electrospun nanofibers as highly efficient flexible SERS substrates, Vib. Spectrosc. 114 (2021) 103246.

[32] Z. Ma, X. Ma, N. Liu, X. Wang, L. Wang, B. Hou, Study on the photocathodic protection of 304 stainless steel by Ag and In_2S_3 co-sensitized TiO_2 composite, Appl. Surf. Sci. 507 (2020) 145088.

[33] C. Zhu, M. Shi, S. Yang, H. Zhang, Z. Yang, B. Ding, Growth of radial arranged TiO_2 nanorods by direct oxidation of Al-coated In-738 superalloy, J. Alloys Compd. 485 (2009) 328-332.

[34] Z. Liu, L. Wang, X. Yu, J. Zhang, R. Yang, X. Zhang, Y. Ji, M. Wu, L. Deng, L. Li, Z.L. Wang, Piezoelectric- Effect- Enhanced Full- Spectrum Photoelectrocatalysis in p–n Heterojunction, Adv. Funct. Mater. 29 (2019) 1807279.

[35] M. Trieloff, E.K. Jessberger, I. Herrwerth, J. Hopp, C. Fiéni, M. Ghélis, M. Bourot-Denise, P. Pellas, Structure and thermal history of the H-chondrite parent asteroid revealed by thermochronometry, Nature, 422 (2003) 502-506.

[36] X. Lu, L. Liu, J. Ge, Y. Cui, F. Wang, Morphology controlled synthesis of $Co(OH)_2$/TiO_2 p-n heterojunction photoelectrodes for efficient photocathodic protection of 304 stainless steel, Appl. Surf. Sci. 537 (2021) 148002.

[37] J. Liu, M. Dai, J. Wu, Y. Hu, Q. Zhang, J. Cui, Y. Wang, H.H. Tan, Y. Wu, Electrochemical hydrogenation of mixed-phase TiO_2 nanotube arrays enables remarkably enhanced photoelectrochemical water splitting performance, Sci. Bull. 63 (2018) 194-202.

[38] Y. Zhang, H. Bao, X. Liu, X. Zhang, H. He, T. Li, H. Yang, S.P. Shah, W. Li, Bi_2S_3 nanoparticles/ZnO nanowire heterojunction films for improved photoelectrochemical cathodic protection for 304 SS under visible light, J. Appl. Electrochem. 52 (2022) 559-571.

[39] M. Sima, E. Vasile, N. Preda, A. Sima, E. Matei, C. Logofatu, Effect of ferroelectric poling on the photoelectrochemical activity of hematite-$BaTiO_3$ nanowire arrays, Int. J. Hydrogen Energy 46 (2021) 36232-36244.

[40] N. Wang, J. Wang, M. Liu, C. Ge, B. Hou, Y. Ning, Y. Hu, Preparation of Ag@$CuFe_2O_4$@TiO_2

nanocomposite films and its performance of photoelectrochemical cathodic protection, J. Mater. Sci. Technol. 100 (2022) 12-19.

[41] N. Wei, Y. Liu, M. Feng, Z. Li, S. Chen, Y. Zheng, D. Wang, Controllable TiO_2 core-shell phase heterojunction for efficient photoelectrochemical water splitting under solar light, Appl. Catal., B 244 (2019) 519-528.

[42] Y. Lei, S. Xu, M. Ding, L. Li, Q. Sun, Z.L. Wang, Enhanced Photocatalysis by Synergistic Piezotronic Effect and Exciton–Plasmon Interaction Based on (Ag- Ag_2S)/$BaTiO_3$ Heterostructures, Adv. Funct. Mater. 30 (2020) 2005716.

[43] X. Lu, L. Liu, X. Xie, Y. Cui, F. Wang, Long-Term Dual Cathodic Protection for Q235 Carbon Steel by $Co(OH)_2$/Graphene/TiO_2 Photocatalytic Material and Traditional Sacrificial Anode, J. Electrochem. Soc. 167 (2020) 131509.

[44] J. Shao, Z.-D. Zhang, X.-T. Wang, X.-D. Zhao, X.-B. Ning, J. Lei, X.-R. Li, B.-R. Hou, Synthesis and Photocathodic Protection Properties of Nanostructured SnS/TiO_2 Composites, J. Electrochem. Soc. 165 (2018) H601-H606.

[45] W. Sun, N. Wei, H. Cui, Y. Lin, X. Wang, J. Tian, J. Li, J. Wen, 3D $ZnIn_2S_4$ nanosheet/TiO_2 nanowire arrays and their efficient photocathodic protection for 304 stainless steel, Appl. Surf. Sci. 434 (2018) 1030-1039.

[46] X. Xie, L. Liu, R. Chen, G. Liu, Y. Li, F. Wang, Long-Term Photoelectrochemical Cathodic Protection by $Co(OH)_2$-Modified TiO_2 on 304 Stainless Steel in Marine Environment, J. Electrochem. Soc. 165 (2018) H3154-H3163.

[47] H. Li, L. Shen, K. Zhang, B. Sun, L. Ren, P. Qiao, K. Pan, L. Wang, W. Zhou, Surface plasmon resonance-enhanced solar-driven photocatalytic performance from Ag nanoparticle-decorated self-floating porous black TiO_2 foams, Appl. Catal., B 220 (2018) 111-117.

[48] A. Boonserm, C. Kruehong, V. Seithtanabutara, A. Artnaseaw, Photoelectrochemical response and corrosion behavior of CdS/TiO_2 nanocomposite films in an aerated 0.5 M NaCl solution, Appl. Surf. Sci. 419 (2017) 933-941.

[49] Z.-C. Guan, X. Wang, P. Jin, Y.-Y. Tang, H.-P. Wang, G.-L. Song, R.-G. Du, Enhanced photoelectrochemical performances of ZnS-Bi_2S_3/TiO_2/WO_3 composite film for photocathodic protection, Corros. Sci. 143 (2018) 31-38.

[50] J. Ren, B. Qian, J. Li, Z. Song, L. Hao, J. Shi, Highly efficient polypyrrole sensitized TiO_2 nanotube films for photocathodic protection of Q235 carbon steel, Corros. Sci. 111 (2016) 596-601.

[51] J. Li, C.-J. Lin, J.-T. Li, Z.-Q. Lin, A photoelectrochemical study of CdS modified TiO_2 nanotube arrays as photoanodes for cathodic protection of stainless steel, Thin Solid Films, 519 (2011) 5494-5502.

[52] J. Zhang, Z. Ur Rahman, Y. Zheng, C. Zhu, M. Tian, D. Wang, Nanoflower like SnO_2-TiO_2 nanotubes composite photoelectrode for efficient photocathodic protection of 304 stainless steel, Appl. Surf. Sci. 457 (2018) 516-521.

[53] J. Hu, Y.-F. Zhu, Q. Liu, Y.-B. Gao, R.-G. Du, C.-J. Lin, SnO_2 Nanoparticle Films Prepared by Pulse Current Deposition for Photocathodic Protection of Stainless Steel, J. Electrochem. Soc. 162 (2015) C161-C166.

[54] N. Wei, Y. Lin, Z. Li, W. Sun, G. Zhang, M. Wang, H. Cui, One-dimensional Ag_2S/ZnS/ZnO nanorod array films for photocathodic protection for 304 stainless steel, J. Mater. Sci. Technol. 42 (2020) 156-162.

[55] X. Zhang, G. Chen, W. Li, D. Wu, Graphitic carbon nitride homojunction films for photocathodic protection of 316 stainless steel and Q235 carbon steel, J. Electroanal. Chem. 857 (2020) 113703.

[56] Y. Yang, Y.F. Cheng, Bi-layered $CeO_2/SrTiO_3$ nanocomposite photoelectrode for energy storage and photocathodic protection, Electrochim. Acta, 253 (2017) 134-141.

[57] H. Zheng, Y. Liu, Y. Zhou, D. Zhao, D. Wang, L. Yun, D. Zhang, L. Zhang, Improved photocathodic protection performance of g-C_3N_4/rGO/ZnS for 304 stainless steel, J. Phys. Chem. Solids 148 (2021) 109672.

[58] H. Li, X. Cui, W. Song, Z. Yang, Y. Li, P. Zhang, Z. Zheng, Y. Wang, J. Li, F. Ma, Direct Z-scheme $MgIn_2S_4/TiO_2$ heterojunction for enhanced photocathodic protection of metals under visible light, Nanotechnology, 33 (2022) 165703.

[59] X. Wang, J. Lei, Q. Shao, X. Li, X. Ning, J. Shao, J. Duan, B. Hou, Preparation of $ZnWO_4/TiO_2$ composite film and its photocathodic protection for 304 stainless steel under visible light, Nanotechnology, 30 (2018) 045710.

[60] Y. He, J. Zhu, Y. Yuan, M. Li, Y. Yang, Y. Liu, M. Chen, D. Cao, X. Yan, Dual-regulation charge separation strategy with the synergistic effect of 1D/0D heterostructure and inserted ferroelectric layer for boosting photoelectrochemical water oxidation, J. Mater. Chem. A 9 (2021) 7594-7605.

[61] Z. Xie, Z. Cui, J. Shi, C. Lin, K. Zhang, G. Yuan, J.M. Liu, Enhancing photoelectrochemical performance of the Bi_2MoO_6 photoanode by ferroelectric polarization regulation, Nanoscale, 12 (2020) 18446-18454.

[62] X. Wu, H. Li, X. Wang, L. Jiang, J. Xi, G. Du, Z. Ji, Ferroelectric enhanced photoelectrochemical water splitting in $BiFeO_3/TiO_2$ composite photoanode, J. Alloys Compd. 783 (2019) 643-651.

[63] J. Wu, N. Qin, D. Bao, Effective enhancement of piezocatalytic activity of $BaTiO_3$ nanowires under ultrasonic vibration, Nano Energy, 45 (2018) 44-51.

[64] P. Wardman, Reduction potentials of one- electron couples involving free radicals in aqueous solution, J. Phys. Chem. Ref. Data 18 (1989) 1637-1755.

[65] Y. Liu, C. Zhao, X. Wang, H. Xu, H. Wang, X. Zhao, J. Feng, W. Yan, Z. Ren, Preparation of PPy/TiO_2 core-shell nanorods film and its photocathodic protection for 304 stainless steel under visible light, Mater. Res. Bull. 124 (2020) 110751.

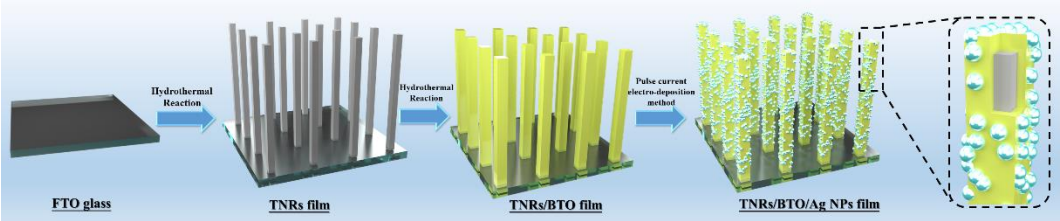

Scheme 1. Schematic illustration of the process of TNRs/BTO/Ag NPs composite synthesis.

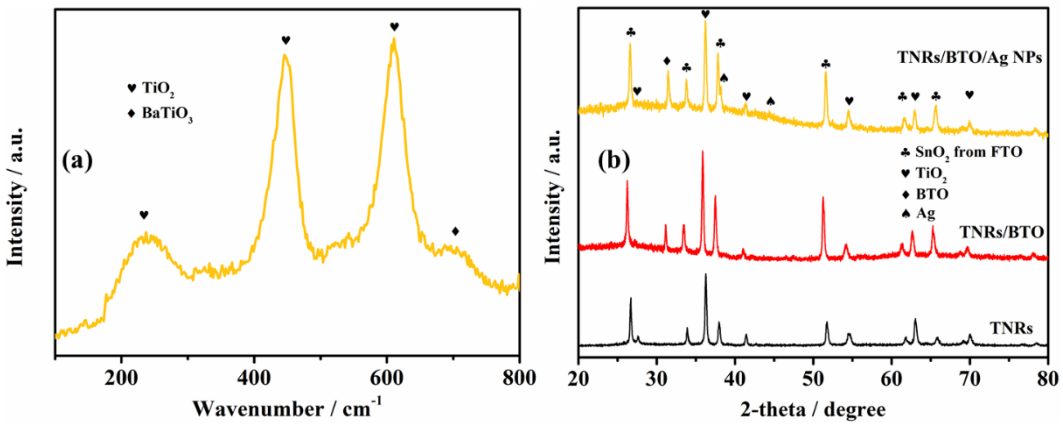

Figure 1. The Raman pattern of TNRs/BTO/Ag NPs (a); The XRD spectra of TNRs, TNRs/BTO and TNRs/BTO/Ag NPs (b);

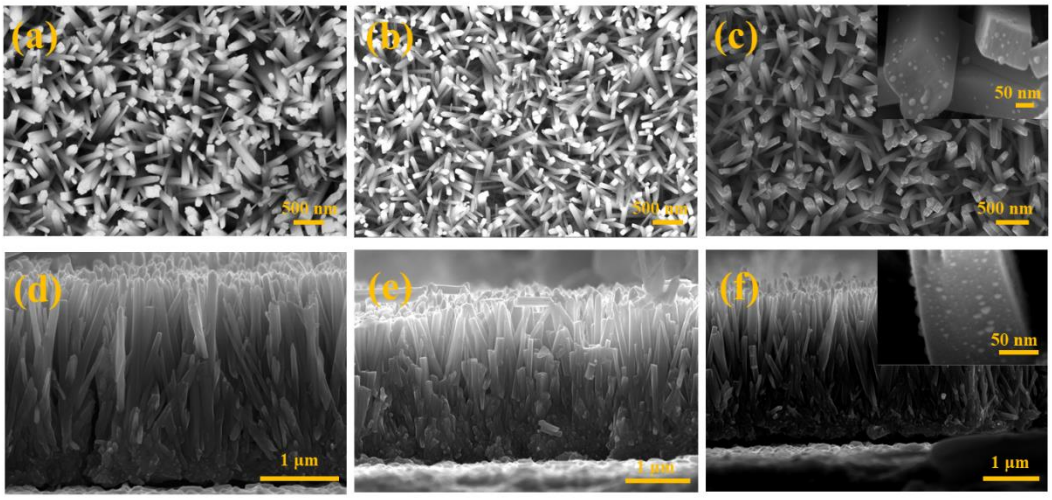

Figure 2. Top-view (a-c) and cross-sectional (d-f) view SEM images of the TNRs (a, d), TNRs/BTO (b, e) and TNRs/BTO/Ag NPs (c, f) composite films.

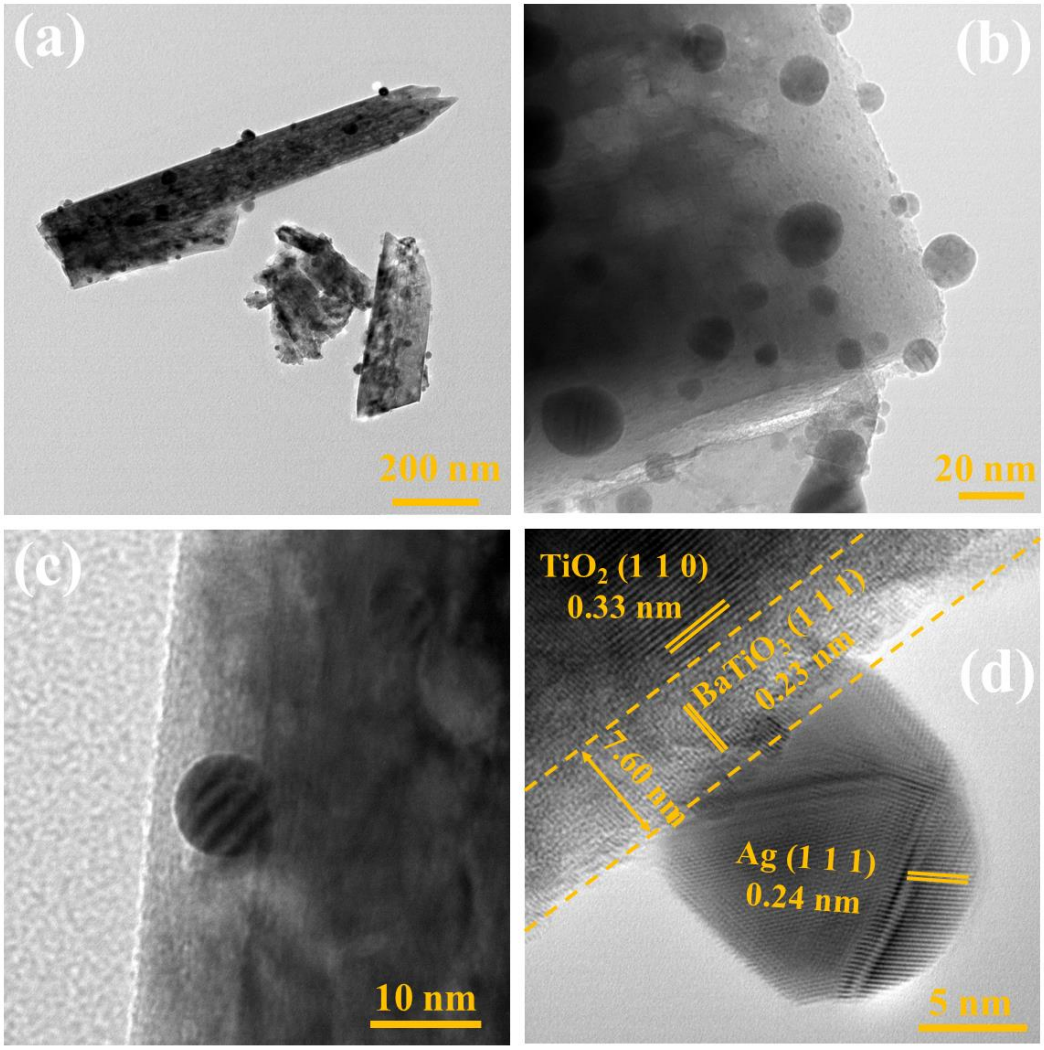

Figure 3. TEM image (a-c) and HRTEM images (d) of TNRs/BTO/Ag NPs composite films.

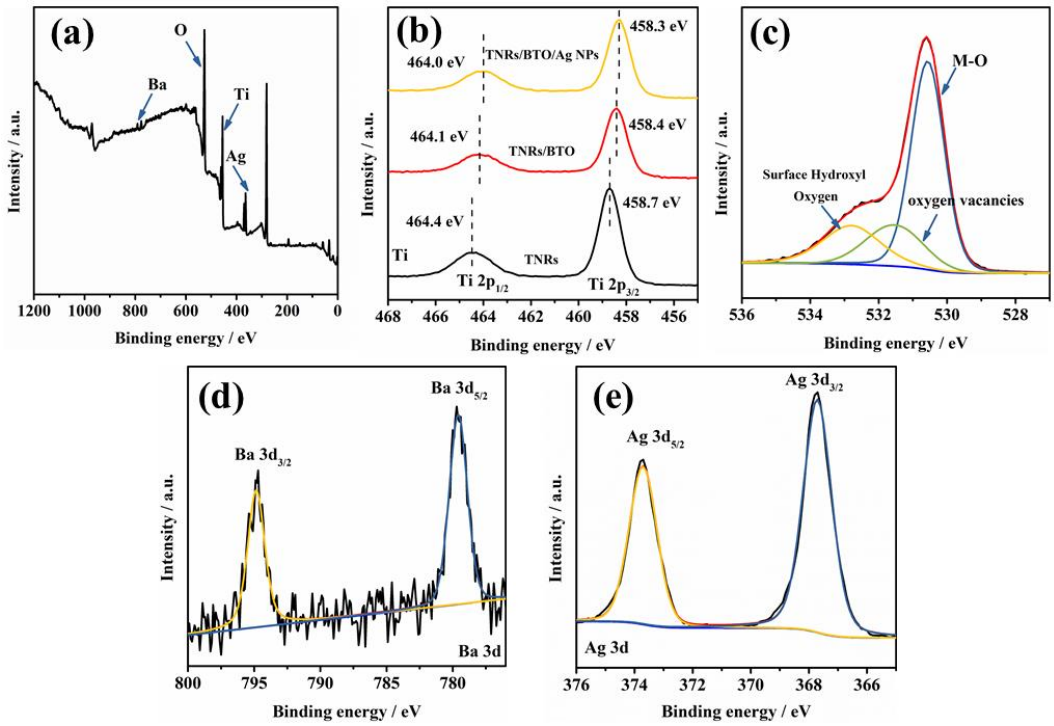

Figure 4. Full scan survey XPS spectrum (a) and high-resolution XPS spectra of O 1s (c), Ba 3d (d) and Ag 3d (e) of TNRs/BTO/Ag NPs composite, and the XPS comparison spectrum of Ti 2p (b) of as-prepared composite.

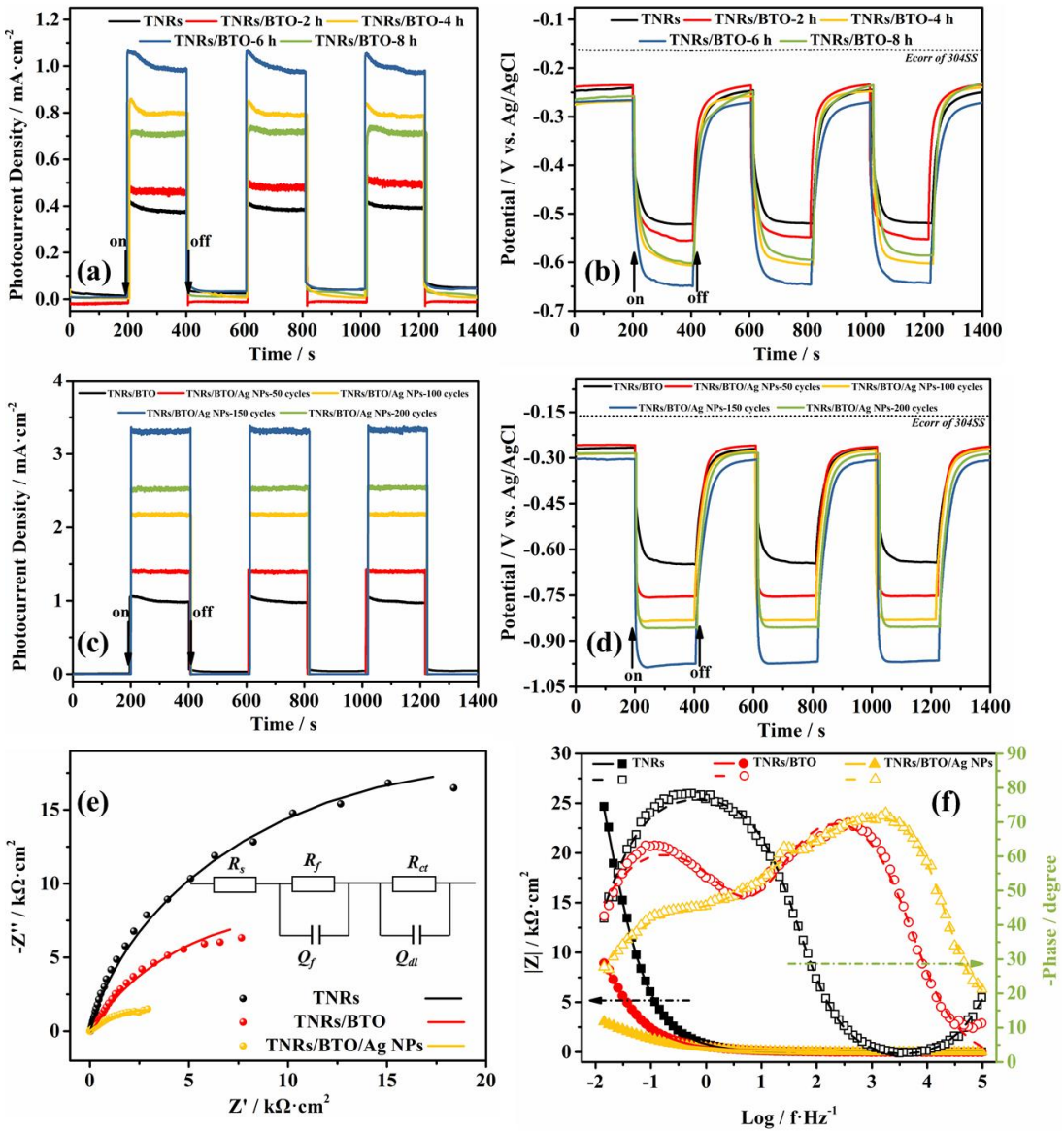

Figure 5. (a and c) The photocurrent density, (b and d) OCP values between the as-prepared composite film in 0.2 M NaOH solution and 304SS electrode in 3.5 wt% NaCl solution with intermittent simulated solar light illumination. (e) Nyquist plots, and (f) Bode-Phase plots of the as-prepared samples in 0.5 M Na_2SO_4 solution with simulated solar light illumination, where the equivalent circuit for fitting the impedance data is also inset in (e).

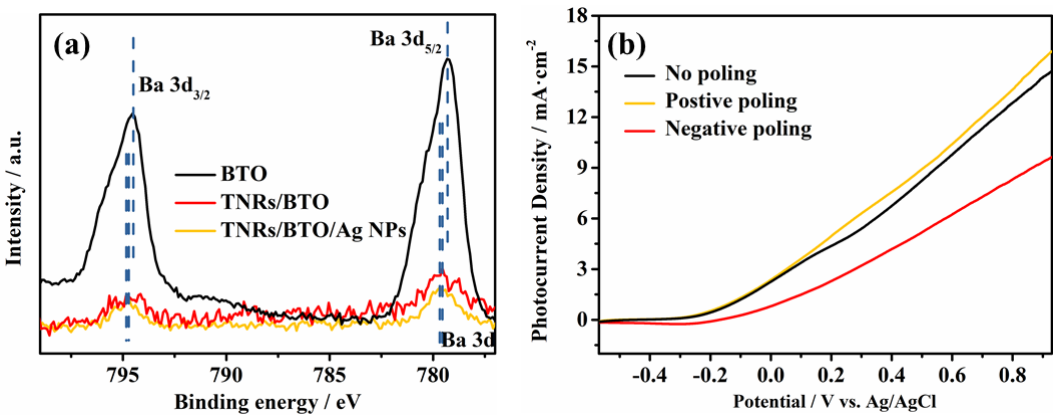

Figure 6. High-resolution XPS spectra (a) of Bs 3d from BTO and TNRs/BTO/Ag NPs; LSV curves (b) of TNRs/BTO/Ag NPs with no poling, positive poling and negative poling

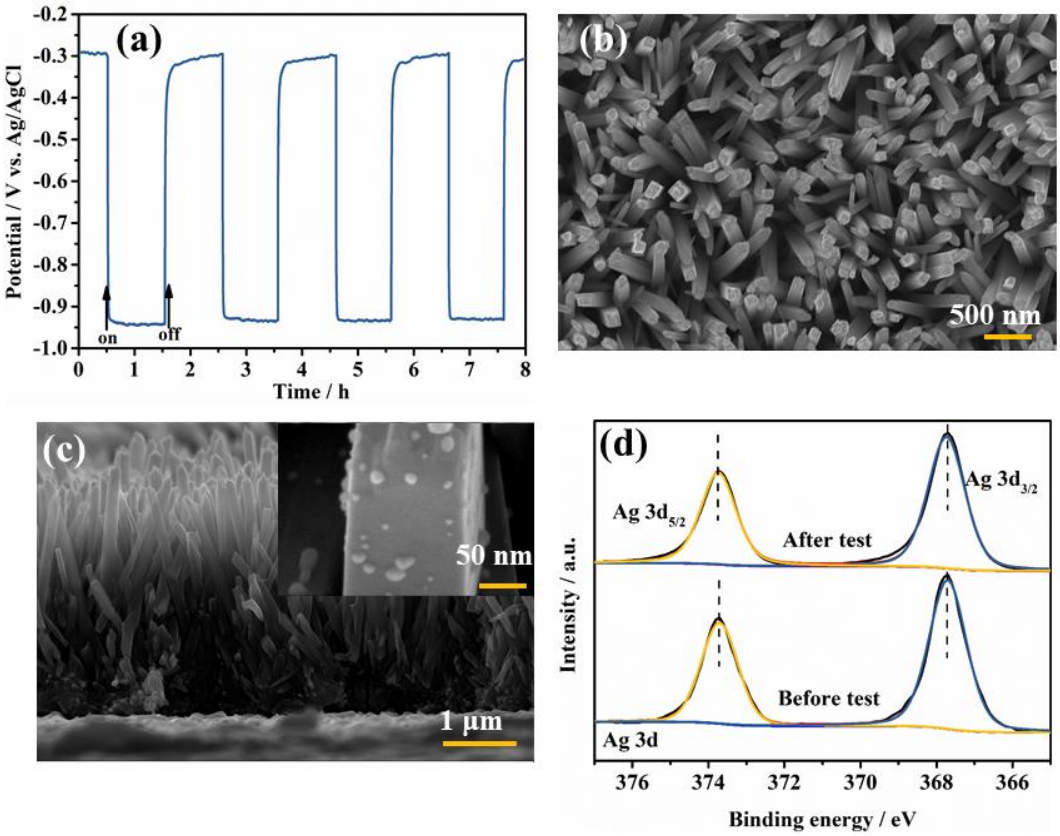

Figure 7. (a) The OCP values of 304SS in 3.5 wt% NaCl solution connected with TNRs/BTO/Ag NPs film in 0.2 M NaOH solution to the light on/off cycles. The top-view (b) and cross-view (c) SEM images of the TNRs/BTO/Ag NPs film after 8 hours' intermittently solar light irradiation. (d) A comparison of exemplified XPS spectra of Ag 3d of the TNRs/BTO/Ag NPs composite film before and after 8 hours' PCP test.

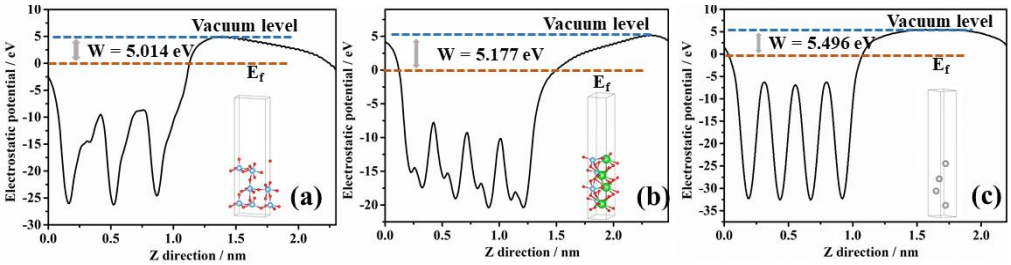

Figure 8. Calculated work functions of Rutile TiO_2 (1 1 0), BTO (1 0 1) and Ag (1 1 1) (a, b, c)

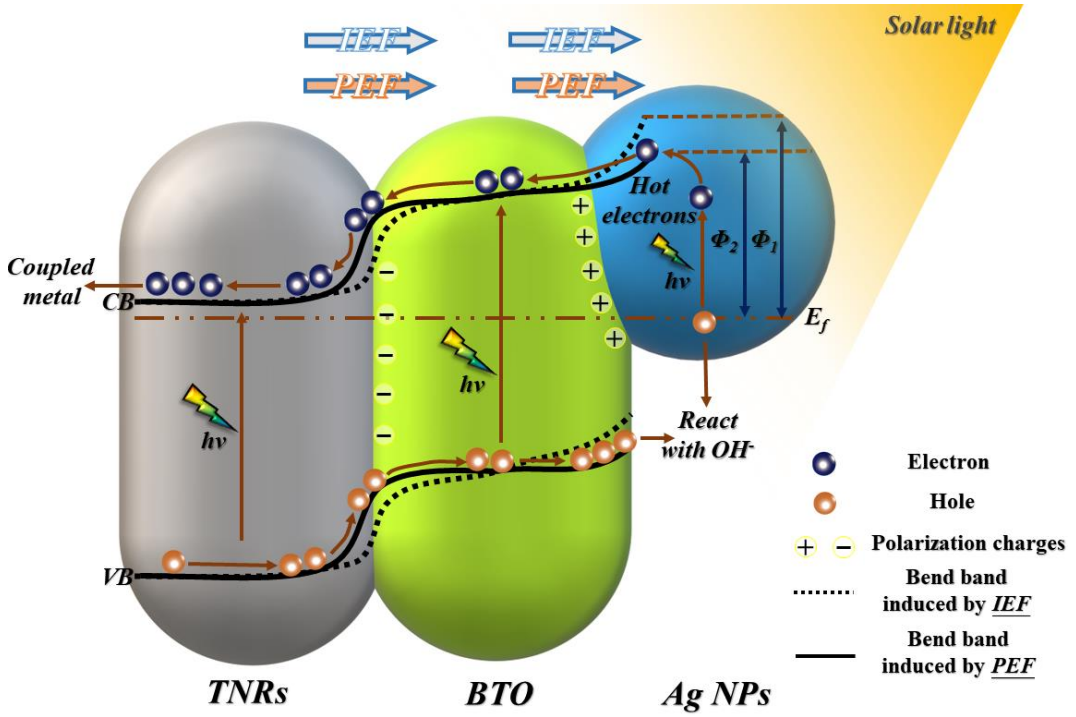

Scheme 2. Mechanism for improved PCP efficiency for the TNRs/BTO/Ag NPs heterostructure under illumination.